Temperature-Dependent Simulations of Dry Gas Transport in the Electrodes of Proton Exchange Membrane Fuel Cells

M. J. Kermani[1]
mkermani@unb.ca

J. M. Stockie[2]
stockie@unb.ca

[1] Post Doctoral Fellow, Department of Mechanical Engineering
[2] Department of Mathematics and Statistics
University of New Brunswick
Fredericton, NB, Canada, E3B 5A3

Abstract

The transport of three gas species, O_2, H_2O and N_2, through the cathode of a proton exchange membrane (PEM) fuel cell is studied numerically. The diffusion of the individual species is modeled via the Maxwell-Stefan equations, coupled with appropriate conservation equations. Two mechanisms are assumed for the internal energy sources in the system: a volumetric heat source due the electrical current flowing through the cathode; and heat flow toward the cathode at cathode-membrane interface due to the exothermic chemical reaction at this interface, in which water is generated. The governing equations of the unsteady fluid motion are written in fully conservative form, and consist of the following: (i) three equations for the mass conservation of the species; (ii) the momentum equation for the mixture, which is approximated using Darcy's Law for flow in porous media; and (iii) an energy equation, written in a form that has enthalpy as the dependent variable.

1   Introduction

Zero emission power generation has always been the ideal goal of people in the power generation community. One approach to achieve this goal is via proton exchange membrane (PEM) fuel cells, which in principle combine oxygen and hydrogen gas in a reaction that generates electrical current, producing only water as a byproduct. A PEM fuel cell consists of two electrodes, the anode (hydrogen supply source) and the cathode (oxygen supply source), between which is sandwiched a polymer membrane, usually consisting of Nafion[®]. The interfaces between the electrodes and membrane are impregnated with a platinum catalyst, as depicted in Fig. 1.

A great deal of recent research has appeared in the liter-
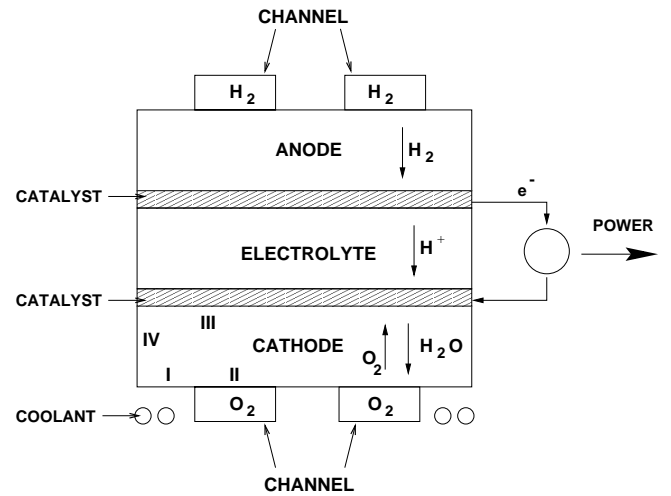
Figure 1: A schematic picture of a proton exchange membrane (PEM) fuel cell.

ature on modeling of transport processes in PEM fuel cells. The vast majority of work (for example, [2], [7], and [11]) has focused on mass transport and it is only more recently that more complete models including heat transport and condensation have appeared (see [3], [6], and [10]).

The present work is part of an ongoing effort to carefully model individual elements of the PEM fuel cell, with a particular focus on simulation of the flow of gas in the porous electrodes. The transport of two species in both anode and cathode was studied in [5], and this work was extended in [8] to handle three species, with $(1, 2, 3) = (H_2, H_2O, CO_2)$ in the anode and $(1, 2, 3) = (O_2, H_2O, N_2)$ in the cathode. These two previous papers assumed isothermal conditions prevailed in the flow domain, whereas an extension of the model to temperature-dependent flows recently appeared in [1], in which the multi-species diffusion

was governed by Fick's Law and temperature was used as the dependent variable in the energy equation.

In this paper, we present a model for gas transport in the cathode that is similar to that developed in [1], except that the full Maxwell-Stefan equations are used for diffusion and enthalpy is used as the independent variable in the energy equation. Our motivation for using enthalpy is that it is a more appropriate quantity for capturing the physics of condensation, which will play an important role in future modeling efforts. First, we validate the numerical model against two test cases: (i) isothermal, three-species flow, and (ii) temperature-dependent two-species flow (for comparison to [1]). Finally, the temperature-dependent algorithm is applied to a three-species flow. In the present work, there is no liquid water, but regions of possible condensation can be identified by considering locations where the partial pressure of H_2O exceeds the steam saturation pressure at the mixture temperature.

2 Mathematical Modeling

2.1 Governing Equations

The governing equations for unsteady flow of a gas mixture composed of three species, $(1, 2, 3) = O_2$, H_2O and N_2, are described here. Three equations for the mass conservation of the species are required, along with momentum and energy equations for the mixture. The momentum equation is approximated by Darcy's Law for flow in porous media, and the energy equation is written in terms of enthalpy in order to simplify future extension of this work to include water condensation.

The conservation equation for the mixture mass can be written as:

$$\frac{\partial \rho}{\partial t} + \nabla \cdot \left[\rho \vec{V} \right] = 0, \tag{1}$$

where ρ and $\vec{V}$ are the mixture density and velocity. For species 1 and 2, the conservation equations are:

$$\frac{\partial C_1}{\partial t} + \nabla \cdot \overbrace{\left[C_1 \vec{V} + \vec{J}_1 \right]}^{N_1} = 0, \tag{2}$$

$$\frac{\partial C_2}{\partial t} + \nabla \cdot \underbrace{\left[C_2 \vec{V} + \vec{J}_2 \right]}_{N_2} = 0, \tag{3}$$

where C_1 and C_2 indicate species molar concentration, and N_1 and N_2 represent the total species fluxes (advective + diffusive). It is important to note that the molar diffusive fluxes $\vec{J}_1$ and $\vec{J}_2$ are measured relative to the mass-averaged velocity $\vec{V}$.

A simplified form of the momentum equation, Darcy's Law for porous media, is assumed to hold in the porous electrode:

$$\vec{V} = -\frac{K}{\epsilon \mu} \nabla P, \tag{4}$$

where μ is the mixture viscosity, and K (permeability) and ϵ (porosity) are characteristics of the porous media.

The energy equation can be written in terms of total enthalpy, $H = h + \frac{V^2}{2}$ as:

$$\frac{\partial}{\partial t} \left(\rho H - P \right) + \nabla \cdot \left[\rho \vec{V} H \right] = -\nabla \cdot \vec{q} + \dot{q}_s \tag{5}$$

where we are operating under low speed conditions in which the work of shear stress can be ignored. The source term arises from two effects, conductive heat flux, diffusive enthalpy fluxes for the multi-species gas mixture, and so can be written as

$$\vec{q} = -\kappa \nabla T + \sum_{i=1}^{3} h_i \, \vec{j}_i = -\kappa \nabla T + \sum_{i=1}^{3} \bar{h}_i \, \vec{J}_i. \tag{6}$$

The specific enthalpy of species i is denoted by h_i, and the mass diffusion flux relative to the mass averaged velocity by $\vec{j}_i = \rho_i (\bar{V}_i - \vec{V})$, where where $\bar{V}_i$ is the velocity of species i, $\vec{V}$ (as noted before) is the mass averaged mixture velocity, and hence $(\bar{V}_i - \vec{V})$ is the species i diffusion velocity. The second form of the diffusive enthalpy term in Eqn. 6 can be derived by making use of the definitions $\bar{h}_i = M_i h_i$ for the molar specific enthalpy and $\vec{J}_i = C_i (\bar{V}_i - \vec{V})$ for the molar diffusive flux relative to the mass-averaged velocity. In Eqn. 5, $\dot{q}_s$ is a volumetric heat source arising from ohmic heat generation

$$\dot{q}_s = \frac{i^2}{\sigma} \tag{7}$$

where i is the electrical current density in the electrode and σ is the electrical conductivity.

For flow in fuel cells, speeds are relatively low and so the kinetic energy is several orders of magnitude smaller than the static enthalpy term. Therefore, H can be approximated as $H = h + \frac{V^2}{2} \approx h$, where

$$h = \frac{\bar{h}}{M} = \frac{\sum_{i=1}^{3} Y_i \, \bar{h}_i}{\sum_{i=1}^{3} Y_i \, M_i}, \tag{8}$$

with M being the mixture molecular weight and Y_i the species mole fraction determined by

$$Y_1 = \frac{C_1}{C}, \qquad Y_2 = \frac{C_2}{C}, \qquad Y_3 = 1 - Y_1 - Y_2. \tag{9}$$

Assuming that all species obey the perfect gas law, in which specific heats can be taken constant near the operating temperature, we then have

$$h = \frac{\left[Y_1 \bar{C}_{p_1} + Y_2 \bar{C}_{p_2} + Y_3 \bar{C}_{p_3}\right] T}{Y_1 M_1 + Y_2 M_2 + Y_3 M_3} \equiv \bar{C}_{p_{av}} T / M \qquad (10)$$

If we also ignore the second term in Eqn. 6, corresponding to the diffusive enthalpy flux of species, then the energy equation for low speed cases becomes

$$\frac{\partial}{\partial t} (\rho h - P) + \nabla \cdot \left[\rho \vec{V} h\right] = \nabla \cdot (\kappa \nabla T) + \frac{i^2}{\sigma} \qquad (11)$$

To close the system of equations, we assume that the mixture obeys the ideal gas law

$$P = C R_0 T, \qquad (12)$$

where R_0 is the universal gas constant. The mixture and species concentrations are related via

$$\rho = \sum_{k=1}^{3} \rho_k = C_1 M_1 + C_2 M_2 + M_3 C_3, \qquad (13)$$

where $C_3 = [C - C_1 - C_2]$ or

$$C = [\rho + (M_3 - M_1) C_1 + (M_3 - M_2) C_2]/M_3. \qquad (14)$$

The auxiliary equations needed to determine the diffusive fluxes, $\vec{J}_1$ and $\vec{J}_2$, are explained in the next section.

2.2 Diffusive Fluxes

The diffusive fluxes, $\vec{J}_k$, are often derived in a simplified form based on Fick's law, which is strictly valid only for mixtures containing two species [9]. A more appropriate model for multi-species diffusion is obtained using the Maxwell-Stefan equations [9]:

$$\begin{bmatrix} \vec{J}_1^* \\ \vec{J}_2^* \end{bmatrix} = -C \underbrace{\begin{bmatrix} D_{11} & D_{12} \\ D_{21} & D_{22} \end{bmatrix}}_{D} \begin{bmatrix} \nabla (C_1/C) \\ \nabla (C_2/C) \end{bmatrix}, \qquad (15)$$

where C is the mixture concentration, D is the matrix of Maxwell-Stefan diffusivities, and $\vec{J}_k^*$ are the molar diffusive fluxes relative to the mole-averaged velocity. The components of D depend on the usual binary diffusivities, Δ_{12}, Δ_{13}, and Δ_{23}, via the relationships

$$\begin{aligned} D_{11} &= \Delta_{13} (Y_1 \Delta_{23} + (1 - Y_1) \Delta_{12}) / S, \\ D_{12} &= Y_1 \Delta_{23} (\Delta_{13} - \Delta_{12}) / S, \\ D_{21} &= Y_2 \Delta_{13} (\Delta_{23} - \Delta_{12}) / S, \\ D_{22} &= \Delta_{23} (Y_2 \Delta_{13} + (1 - Y_2) \Delta_{12}) / S, \qquad (16) \end{aligned}$$

where

$$S = Y_1 \Delta_{23} + Y_2 \Delta_{13} + Y_3 \Delta_{12}. \qquad (17)$$

The diffusive fluxes based on mole- and mass-averaged velocities, i.e. $\vec{J}_i^*$ and $\vec{J}_i$, are connected via the following relationship [9]:

$$\begin{bmatrix} \vec{J}_1 \\ \vec{J}_2 \end{bmatrix} = S \begin{bmatrix} \vec{J}_1^* \\ \vec{J}_2^* \end{bmatrix} \equiv \begin{bmatrix} s_{11} & s_{12} \\ s_{21} & s_{22} \end{bmatrix} \begin{bmatrix} \vec{J}_1^* \\ \vec{J}_2^* \end{bmatrix}, \qquad (18)$$

where the components of the conversion matrix S are

$$s_{kl} = \delta_{kl} - \frac{C_k M_k}{\rho} \left(1 - \frac{M_3}{M_l}\right), \quad k, l = 1, 2, \qquad (19)$$

where $\delta_{kl} = 1$ if $k = l$, and $\delta_{kl} = 0$ if $k \neq l$.

Combining Eqns. 15 and 18 yields

$$\begin{bmatrix} \vec{J}_1 \\ \vec{J}_2 \end{bmatrix} = - \begin{bmatrix} a & b \\ c & d \end{bmatrix} \begin{bmatrix} \nabla (C_1/C) \\ \nabla (C_2/C) \end{bmatrix}, \qquad (20)$$

where

$$\begin{aligned} a &= C [s_{11} D_{11} + s_{12} D_{21}] \\ b &= C [s_{11} D_{12} + s_{12} D_{22}] \\ c &= C [s_{21} D_{11} + s_{22} D_{21}] \\ d &= C [s_{21} D_{12} + s_{22} D_{22}]. \qquad (21) \end{aligned}$$

The final diffusivity matrix D is scaled by a factor of $\epsilon^{1.5} \approx 0.636$, known as a Bruggeman correction, in order to take in to account the resistance to diffusion due to the porous medium.

2.3 Discretization of Governing Equations

We now take the velocity from Darcy's Law,

$$\vec{V} = - \underbrace{\frac{K}{\epsilon \mu}}_{B_0} \nabla P \equiv -B_0 \nabla P \qquad (22)$$

and substitute into Eqns. 1, 2, 3, and 11, which yields

$$\frac{\partial \rho}{\partial t} = \nabla \cdot (\rho B_0 \nabla P), \qquad (23)$$

$$\frac{\partial C_1}{\partial t} = \nabla \cdot \left[C_1 B_0 \nabla P - \vec{J}_1\right], \qquad (24)$$

$$\frac{\partial C_2}{\partial t} = \nabla \cdot \left[C_2 B_0 \nabla P - \vec{J}_2\right], \qquad (25)$$

$$\frac{\partial}{\partial t} (\rho h - P) = \nabla \cdot (\rho B_0 h \nabla P) + \nabla \cdot (\kappa \nabla T) + \frac{i^2}{\sigma}. \qquad (26)$$

The above equations are discretized using a cell-vertex finite volume approach, in which all flow parameters are stored at cell vertices. This approach allows us to locate

nodes on the boundaries of the computational domain. In the description that follows, we represent a typical temporal derivative term by $\partial Q / \partial t$, and spatial derivatives by $\partial F / \partial x$, where F is of the form $F = A(\partial B / \partial x)$ in all cases. Time derivatives are integrated using a first order explicit scheme, while spatial derivatives are discretized via second order centered differences, suitable for the diffusion terms:

$$\left(\frac{\partial F}{\partial x} \right)_{j,k} = \frac{1}{\Delta x} \left[F_E - F_W \right], \qquad (27)$$

where F_E, and F_W are the numerical fluxes at the East (E) and West (W) faces of a control volume surrounding node (j,k). F_E and F_W are determined from

$$F_E = \frac{1}{2\Delta x} \left[A_{j+1,k} + A_{j,k} \right] \left[B_{j+1,k} - B_{j,k} \right], \qquad (28)$$

$$F_W = \frac{1}{2\Delta x} \left[A_{j,k} + A_{j-1,k} \right] \left[B_{j,k} - B_{j-1,k} \right], \qquad (29)$$

and similarly for the y-derivative terms.

2.4 Boundary Conditions

For the following discussion of boundary conditions, refer to Fig. 1. At boundary locations (I), the wall is assumed to be impermeable. That is, $J_1^y = J_2^y = 0$, and $v = 0$, where J_k^y and v represent flux and velocity components in vertical direction. The heat flux conducted through this boundary is determined by an equivalent convective heat flux from the coolant, written as $\kappa(\partial T / \partial y) = K_T^W (T - T^W)$, where K_T^W is an equivalent convective heat transfer coefficient between the electrode and coolant, and T_W is the coolant temperature.

At open channel boundary (II), the gas pressure is set equal to the channel pressure, $P = \bar{P}$. The diffusive fluxes at this boundary are assumed to obey a mass flux condition of the form $N_k^y \approx J_k^y = r_0^k (\bar{C}_k - C_k)$, for $k = 1, 2$, where r_0^k is the convective mass transfer coefficient for species k. Ignoring advective terms in the energy equation at this boundary, the energy balance is approximated by $\kappa(\partial T / \partial y) = K_T^C (T - \bar{T})$, where K_T^C is the convective heat transfer coefficient in the channel and $\bar{T}$ is the (constant) channel temperature.

At the catalyst boundary (III), species 1 (O_2) is assumed to obey the mass flux condition $N_1^y \approx J_1^y = r_H (C_1 - C_\infty)$, where r_H is the convective mass transfer coefficient, and C_∞ is the concentration at the membrane, usually taken equal to be zero. Water vapor (species 2) is generated at this boundary at the rate of two moles of water for each mole of oxygen that crosses the cathode-catalyst boundary; hence, $N_2^y = -2N_1^y$. The inert gas component, species 3 (N_2), cannot penetrate the membrane which is impermeable to gas, and so $N_3^y = 0$. A
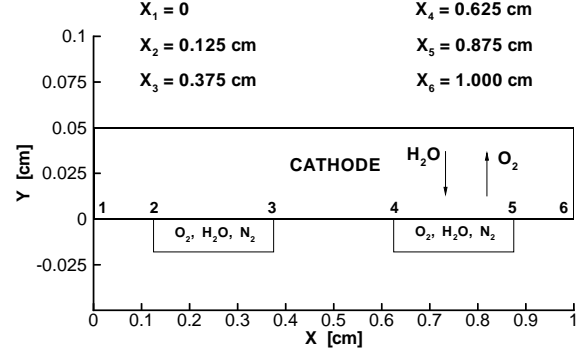
Figure 2: Computational domain, consisting of a 2D slice through the cathode over a pair of flow channels.

heat flux arises at this boundary due to the heat of reaction, and hence $\kappa(\partial T / \partial y) = 2N_1^y h_r$, where h_r is the enthalpy of formation of water in gas form.

At side boundaries (IV), periodic boundary conditions are specified.

3 Results and Discussions

3.1 Numerical Validation

In this section, we present three simulations of gas transport in a fuel cell cathode: the first two for the purposes of numerical validation of the model versus previous results; and the final one being a full three-species non-isothermal computation.

3.1.1 Three Species Isothermal Computation

The first validating test case we perform relates to isothermal flow of a three species $(1, 2, 3) = (O_2, H_2O, N_2)$ mixture in the cathode, governed by Eqns. 23–25, in order to compare with the results reported in Stockie et al. [8]. In this paper, the governing equations were discretized using a method of lines approach, and resulting system of ordinary differential equations were integrated implicitly using the stiff ODE solver of DASSL.

The computational domain is depicted in Fig. 2, and the parameters, taken from [8], are as follows: permeability ($K = 10^{-8}~cm^2$), porosity ($\epsilon = 0.74$), viscosity ($\mu = 2.24 \times 10^{-4}$ g/(cm . s)), binary diffusivities ($\Delta_{12} = 0.124$, $\Delta_{13} = 0.104$, and $\Delta_{23} = 0.123~cm^2/s$), channel pressure ($\bar{P} = 1.0 \times 10^6~dyne/cm^2$), species mole fractions in the channel ($Y_1 = 0.21$, $Y_2 = 0.10$, and $Y_3 = 69$), channel temperature ($\bar{T} = 346.15^o K$), and mass transfer coefficients ($r_0^1 = r_0^2 = 10~cm/s$ and $r_H = 0.8~cm/s$).
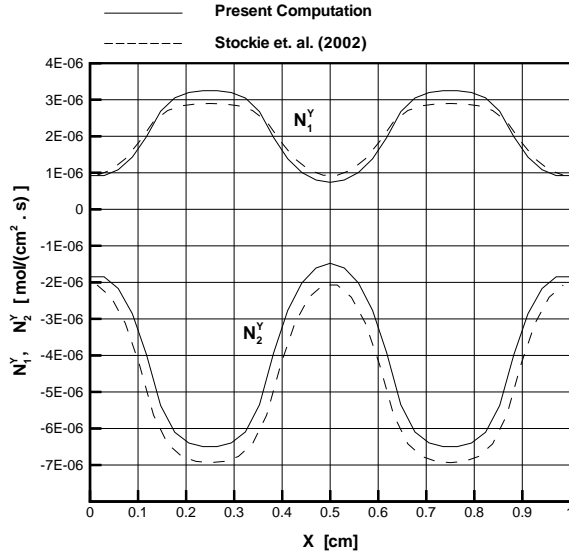
Figure 3: Comparison of molar fluxes at the top boundary for species $(1,2) = (O_2, H_2O)$ with the results in [8].
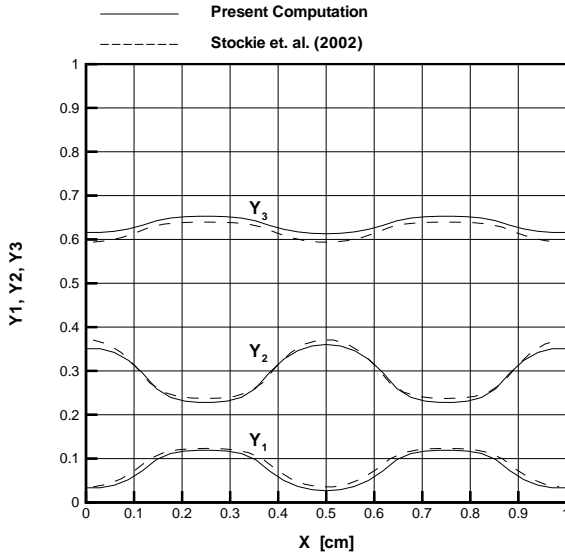
Figure 4: Comparison of computed mole fractions at the catalyst boundary for species $(1,2,3) = (O_2, H_2O, N_2)$ with the results in [8].
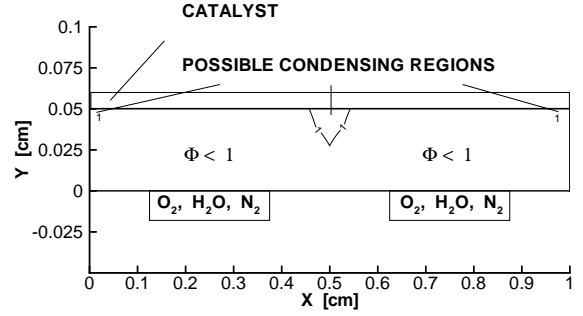
Figure 5: Regions of possible condensation predicted by the model, assuming isothermal conditions.

Figs. 3 and 4 displays the results of the present computation in terms of the steady-state oxygen and water fluxes at the catalyst layer (i.e., the top boundary). The difference in molar fluxes at the peaks or valleys differ by at most 7.1%. The agreement in mole fractions is considerably better, lying within about 1%.

In the present computation, neither phase change nor condensation is modeled. However, the regions in which condensation are likely to occur can still be estimated as follows. Condensation occurs at the dew point, where the partial pressure of water vapor, P_v, reaches the saturation pressure at the mixture temperature, i.e. $P_v/P_{sat}(T) \to 1$. With this in mind, we define a new parameter called the relative humidity, $\Phi = P_v/P_{sat}(T)$, where the saturation pressure P_{sat} is determined as in Appendix A. $\Phi < 1$ represents dry regions, and while Φ cannot exceed 1 in an actual condensation problem, we identify regions in which condensation is occurring by $\Phi \geq 1$ in the present dry computations.

Under usual fuel cell operating conditions, liquid water is known to be generated, but the exact location where condensation occurs is unknown. If water condenses on or near the catalyst layer (where the product H_2O enters the cathode), then pockets of water may collect which could potentially narrow the channels through which oxygen gas is supplied to the catalyst. In turn, these pockets of water could restrict or interrupt the supply of oxygen to the catalyst and thereby degrade fuel cell performance. As a result, management of liquid water is of prime importance in fuel cells, and identifying the locus $\Phi = 1$ is a first step in locating potential problem situations.

Fig. 5 shows the condensation pockets predicted by the isothermal simulation, which occur at the catalyst boundary. Clearly, the supply of reactant gases are not cut off in this case, but there is a potential for performance degradation if excessive water is generated in these pockets, which
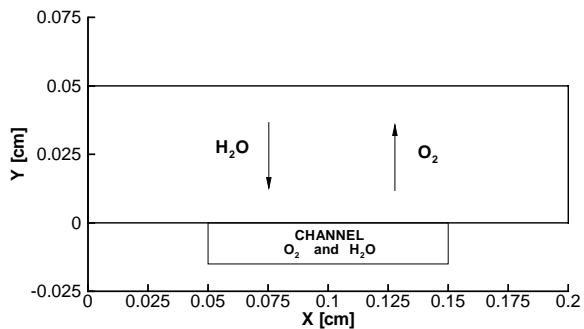
Figure 6: Fuel cell used by Bradean et al. [1].

could cause regions of the catalyst to be starved of oxygen.

3.1.2 Two Species Non-Isothermal Computation

In the remaining two simulations, we consider the full set of governing equations, including the energy equation 26. This section deals with a non-isothermal computation of two-species flow (i.e. O_2, H_2O) in the cathode, corresponding to an example considered by Bradean et al. [1]. In their computation, the governing equations were written in steady form, and a pressure-based scheme due to [4] is employed to iterate on the solution until convergence is obtained. Furthermore, a single-channel geometry was studied (see Fig. 6). It should also be noted that in their computations, the two-species mixture was assumed to obey Fick's Law; our model, on the other hand, has three gas species modeled by the Maxwell-Stefan, and so we have set the concentration of the third species, N_2, to zero for comparison purposes.

The problem parameters used in this case are as follows: permeability ($K = 10^{-8}$ cm^2), porosity ($\epsilon = 0.74$), viscosity ($\mu = 2.24 \times 10^{-4}$ g/(cm . s)), effective diffusivity ($D = 0.08$ cm^2/s)*, effective thermal conductivity ($\kappa = 4. \times 10^5$ $erg/(s \ cm \ ^oK)$), specific heat of the mixture ($C_p = 2. \times 10^7$ $erg/(g \ ^oK)$), channel pressure ($\bar{P} = 1.1 \times 10^6$ $dyne/cm^2$), mass fraction of O_2 ($\rho_{O_2}/\rho = 0.71$)†, channel and coolant temperatures ($\bar{T} = T^W = 353.15^oK$), channel mass transfer coefficient ($r_0^1 = 800$ cm/s), channel convective heat transfer coefficient ($K_T^C = 1.5 \times 10^4$ $erg/(s \ cm^2 \ ^oK)$), equivalent convective heat transfer coefficient in graphite ($K_T^W = 1.1 \times 10^7$ $erg/(s \ cm^2 \ ^oK)$), heat of reaction ($h_r = 1.36 \times 10^{12}$ erg/mol), and mass transfer coefficient

---

*Based on binary diffusivity values of $\Delta_{12} = 0.124$, $\Delta_{13} = 0.104$, and $\Delta_{23} = 0.123$ cm^2/s.

†The channel mass fractions were converted to equivalent mole fractions of $Y_1 = 0.58$, $Y_2 = 0.42$, and $Y_3 = 0$.
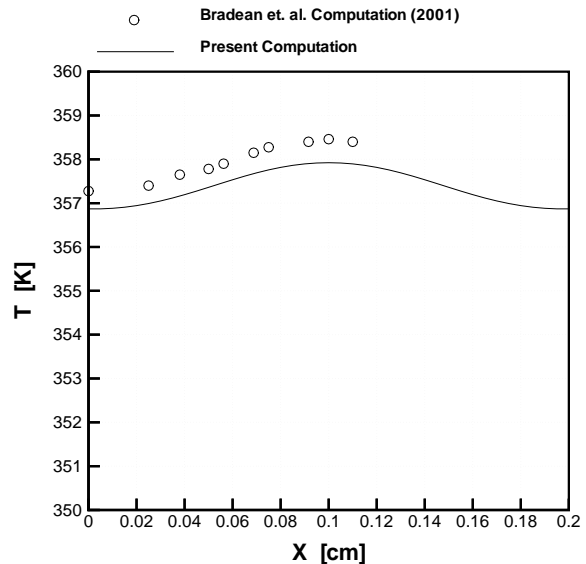
Figure 7: Comparison of temperature distribution at the catalyst boundary (the top boundary) with the results in [1].

at the catalyst ($r_H = 0.3$ cm/s).

The numerical results for this example are displayed in Figs. 7 and 8. The computed temperatures agree to within approximately 0.6^oK and the location of the condensation region depicted in Fig. 8 also matches very well with the results reported in [1].

3.2 Three Species Non-Isothermal Computation

In this section, we present simulations of a full three-species non-isothermal flow, and compare the results to an equivalent isothermal calculation. The problem parameters used in this non-isothermal case are: $\kappa = 0.677 \times 10^5 erg/(cm \ s \ ^oK)$, $\bar{C}_{p_{O_2}}$, $\bar{C}_{p_{H_2O}}$, $\bar{C}_{p_{N_2}}$ respectively $= 2.97 \times 10^8$, 3.39×10^8, and 2.91×10^8 $erg/(mol.^oK)$, $K_T^C = 1.5 \times 10^5$ $erg/(s \ cm^2 \ ^oK)$, $K_T^W = 1.1 \times 10^7$ $erg/(s \ cm^2 \ ^oK)$, $T^W = 346.15^oK$, $h_r = 2.418 \times 10^{12}$ erg/mol, $i = 1.0$ amp/cm^2, and $\sigma = 7.273 \times 10^{-5}$ $amp^2 s/(erg \ cm)$. The rest of parameters were similar to the test case of Section 3.1.1.

The $\Phi = 1$ contour in Fig. 9 shows that the electrode remains almost totally dry except for a small pocket of condensation that appears at the bottom boundary above the landing area (the solid wall region separating the two channels). This prediction runs contrary to the results from the isothermal case, in which condensing pockets appear along the top boundary (see Figs. 5 and 9). This significant change in the location of the condensing regions highlights the importance of solving the energy equation
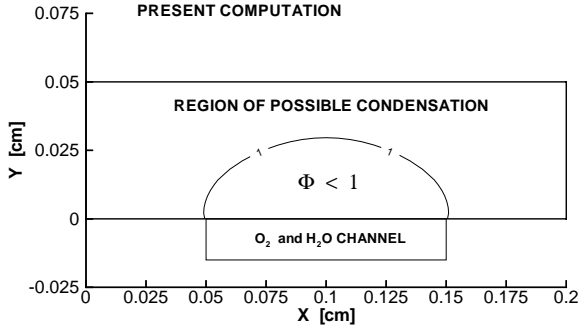
Figure 8: Region of possible condensation predicted by the present two species non-isothermal computation with one channel.
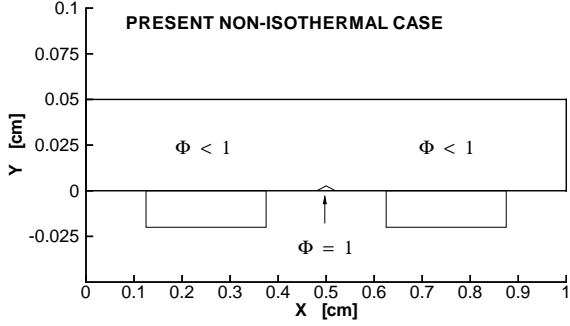
Figure 9: Region of possible condensation predicted by the present three species non-isothermal computation with two channel.

Figure 10: Comparison of three-species isothermal (left) and non-isothermal (right) computations.

along with the other transport equations.

The two sets of results are compared in Fig. 10 along horizontal cross-sections at both the upper and lower boundaries. Figures 10-a, and b show the distribution of the relative humidity, Φ, along the top and bottom boundaries, where $\Phi = P_v/P_{sat}$ and P_{sat} is given by Eqn. 30. Uniform temperature in the isothermal case corresponds to a constant value of saturation pressure. In the non-isothermal case, the temperature field is perturbed via two sources: (i) heat source terms, arising from $\dot{q}_s$ in the energy equation; and (ii) the heat of reaction at the catalyst boundary which enters the electrode from the top boundary. The heat of reaction requires that the temperature at the catalyst boundary be the highest along any horizontal cross-section, as evidenced in Fig. 10-f. Furthermore, a maximum temperature variation of about $8.0^o K$ was obtained along the vertical cross-section at mid-channel ($x = 0.25$ cm). While this temperature variation seems somewhat large in view of the $0.5\ mm$ thickness of the

electrode. A milder temperature variation could be obtained, for example, by choosing a material with higher thermal conductivity. A test case has been performed using a $\kappa = 4 \times 10^5\ erg/(cm\ s\ ^oK)$ (about 6 times larger thermal conductivity) and a temperature variation of less

than 1.0^oK was obtained across the electrode. These results are not included in here because of space limitations.

We can also use the results of Fig. 10 to explain why the condensing regions migrate from the upper catalyst boundary to the bottom boundary. In Fig. 10-f, the temperature variation along the vertical cross section $x = 0.5\,cm$ is approximately 5.0^oK, which translates into a rise of $\Delta P_{sat} = 6.21 \times 10^4\,dyne/cm^2$ (or about 17% of local saturation pressure). This ΔP_{sat} is the main reason that the Φ decreases as we move upward through the electrode above the landing area. It is noted that the main variation in Φ is due to P_{sat}, because of the similarity between mole fraction (Y_2) and mixture pressure (P) between the isothermal and non-isothermal cases (see Figs. 10-c, d, i, and j).

4 Conclusion

A mathematical model is presented for simulating isothermal flow of three gas species (O_2, H_2O and N_2) in the cathode of a proton exchange membrane fuel cell. The three transport equations for the three species are augmented by an energy equation in order to determine the temperature variations in the electrode. Regions of possible condensation are obtained using this model by monitoring the over-saturated regions. We demonstrate that only slight variations in temperature throughout the domain (of about 5.0^oK) can significantly change the location of regions of condensing gas.

The energy equation is written in terms of enthalpy as the dependent variable, which will be an important issue in future studies that focus on careful modeling of condensation and liquid water management.

Acknowledgment

Appendix A

The saturation pressure for steam, within a temperature range of $T = [40, 160]^oC$, is determined from the following polynomial of degree 5 in terms of $dyne/cm^2$:

$$P_{sat}(T) = a\,T^5 + b\,T^4 + c\,T^3 + d\,T^2 + e\,T + f, \quad (30)$$

where

$$a = 7.79E - 6, \quad b = +1.06E - 2, \quad c = -9.84E - 1$$

$$d = 1.13E + 2, \quad e = -3.43E + 3, \quad f = +6.60E + 4$$

Thermodynamic data is taken from steam thermodynamic data and fitted using a fifth-order, least squares polynomial approximation.

References

[1] Bradean, R. P., Promislow, K., and Wetton, B. R. Heat and mass transfer in porous fuel cell electrodes. In *Proceedings of the International Symposium on Advances in Computational Heat Transfer*, Queensland, Australia, May 2001.

[2] Gurau, V., Liu, H., and Kakaç, S. Two-dimensional model for proton exchange membrane fuel cells. *AIChE J.*, 44(11):2410–2422, 1998.

[3] He, W., Yi, J. S., and Nguyen, T. V. Two-phase flow model of the cathode of PEM fuel cells using interdigitated flow fields. *AIChE J.*, 46(10):2053–2064, 2000.

[4] Patankar, S. V. Numerical Heat Transfer and Fluid Flow. Hemisphere, Washington DC, 1980.

[5] Promislow, K., and Stockie, J. M. Adiabatic relaxation of convective-diffusive gas transport in a porous fuel cell electrode. *SIAM J. Appl. Math.*, 62(1): 180–205, 2001.

[6] Rowe, A., and Li, X. Mathematical modeling of proton exchange membrane fuel cells. *J. Power Sources*, 102:82–96, 2001.

[7] Singh, D., Lu, D. M., and Djilali, N. A two-dimensional analysis of mass transport in proton exchange membrane fuel cells. *Internat. J. Eng. Sci.*, 37:431–452, 1999.

[8] Stockie, J. M., Promislow, K. and Wetton, B. R. A finite volume method for multicomponent gas transport in a porous fuel cell electrode. Submitted.

[9] Taylor, R., and Krishna, R. Multicomponent Mass Transfer. John Wiley and Sons, New York, 1993.

[10] Wang, Z. H., Wang, C. Y., and Chen, K. S. Two-phase flow and transport in the air cathode of proton exchange membrane fuel cells. *J. Power Sources*, 94(1):40–50, 2001.

[11] Yi J. S., and Nguyen, T. V. Multicomponent transport in porous electrodes of proton exchange membrane fuel cells using the interdigitated gas distributors. *J. Electrochem. Soc.*, 146(1):38–45, 1999.